

# Fine structures of acoustic emission spectra: How to separate dislocation movements and entanglements in 316L stainless steel

Cite as: Appl. Phys. Lett. **117**, 262901 (2020); <https://doi.org/10.1063/5.0030508>

Submitted: 22 September 2020 . Accepted: 12 December 2020 . Published Online: 28 December 2020

Yan Chen, Boyuan Gou, Wei Fu, Can Chen,  Xiangdong Ding, Jun Sun, and  Ekhard K. H. Salje



View Online



Export Citation



CrossMark

## ARTICLES YOU MAY BE INTERESTED IN

[Identifying alternative ferroelectric materials beyond Hf\(Zr\)O<sub>2</sub>](#)

Applied Physics Letters **117**, 262903 (2020); <https://doi.org/10.1063/5.0028611>

[Polarization switching in thin doped HfO<sub>2</sub> ferroelectric layers](#)

Applied Physics Letters **117**, 262904 (2020); <https://doi.org/10.1063/5.0035100>

[Determination of carbon-related trap energy level in \(Al\)GaN buffers for high electron mobility transistors through a room-temperature approach](#)

Applied Physics Letters **117**, 263501 (2020); <https://doi.org/10.1063/5.0031029>



## Your Qubits. Measured.

Meet the next generation of quantum analyzers

- Readout for up to 64 qubits
- Operation at up to 8.5 GHz, mixer-calibration-free
- Signal optimization with minimal latency

Find out more



# Fine structures of acoustic emission spectra: How to separate dislocation movements and entanglements in 316L stainless steel

Cite as: Appl. Phys. Lett. **117**, 262901 (2020); doi: 10.1063/5.0030508

Submitted: 22 September 2020 · Accepted: 12 December 2020 ·

Published Online: 28 December 2020



View Online



Export Citation



CrossMark

Yan Chen,<sup>1,2</sup> Boyuan Gou,<sup>1</sup> Wei Fu,<sup>1</sup> Can Chen,<sup>1</sup> Xiangdong Ding,<sup>1,a)</sup>  Jun Sun,<sup>1</sup> and Ekhard K. H. Salje<sup>1,2,a)</sup> 

## AFFILIATIONS

<sup>1</sup>State Key Laboratory for Mechanical Behavior of Materials, Xi'an Jiaotong University, Xi'an 710049, China

<sup>2</sup>Department of Earth Sciences, University of Cambridge, Cambridge CB2 3EQ, England

<sup>a)</sup>Authors to whom correspondence should be addressed: [dingxd@mail.xjtu.edu.cn](mailto:dingxd@mail.xjtu.edu.cn) and [ekhard@esc.cam.ac.uk](mailto:ekhard@esc.cam.ac.uk)

## ABSTRACT

Intermittent avalanches in a multitude of materials are characterized by acoustic emission, AE, where local events lead to strain relaxations and generate shock waves (so-called “jerks”), which are measured at the sample surface. The bane of this approach is that several avalanche mechanisms may contribute to the same AE spectrum so that a detailed analysis of each individual contribution becomes virtually impossible. It is, hence, essential to develop tools to separate signals from different dynamical processes, such as ferroic domain switching, collapse of porous inclusions, dislocation movements, entanglements, and so on. Particularly, difficult cases are dynamical microstructures in fcc alloys where the AE signal strength is weak. Nevertheless, using profile analysis of AE signals, we can distinguish between two mechanisms, namely, dislocation movements and dynamic entanglements in fcc 316L stainless steel. In this approach, we are able to measure the statistical AE durations of both subsets separately. The fingerprint for superposed avalanches with different durations is seen by the scaling between the energy  $E$  and the maximum amplitude  $A$  of each avalanche  $E \sim A^x$  with  $x = 2$ . While the same exponent  $x$  applies for both mechanisms, the scaling relation shows two branches with different absolute energy values. The two mechanisms are then confirmed by separating the energy distributions  $P(E) \sim E^{-\varepsilon}$  for the two mechanisms with  $\varepsilon = 1.55$  for dislocation movements and  $\varepsilon = 1.36$  for entanglements.

Published under license by AIP Publishing. <https://doi.org/10.1063/5.0030508>

Elastic, yield, and plastic deformations in alloys and ferroic switching movements are promoted by collective dynamic phenomena such as displacement avalanches. Various experimental tools are commonly used to observe avalanches. One of the most reliable detection methods is the measurement of acoustic emission, AE. Brittle alloys show macroscopically very rich AE signals during deformation. AE spectra (i.e., the power spectra of acoustic emission) can contain well over a million jerk events.<sup>1–13</sup> Very intense AE signals are commonly observed in porous materials under stress,<sup>14–22</sup> while AE signals in alloys, such as steel, Cu, and Ni, are more sparse.<sup>23,24</sup>

Common to all these observations is that structural changes during deformation of an alloy are not simply individual movements but that all changes happen collectively during avalanches. Characteristic avalanche parameters (their energies, amplitudes, waiting times, and durations) show typically power laws as probability distribution functions.<sup>7,8,14,25,26</sup> This means that structural changes are scale invariant, i.e., they happen with the same probability distribution independently

of their energy, timescale, or amplitude. Furthermore, we find that the internal scaling between the avalanche parameters often fulfills the prediction of mean field, MF, theory<sup>26,27</sup> with energy exponents close to either the MF value at criticality of 1.33 or the force integrated MF value of 1.66. The avalanche analysis was then advanced in two ways. First, it was realized that the power law exponents show a significant time evolution with a typical decrease prior to critical failure points<sup>28</sup> and a simultaneous increase in AE activities. Such precursor phenomena are important to understand pico-seismicity in coalmines and boreholes, collapsing buildings, mining industry, etc. In experimental terms, such precursor avalanches were detected via “super-jerks” that exceed the energy of all previous AE signals.<sup>29,30</sup> The second advance is related to the physical origin for jerk spectra. It was discovered that jerk spectra may contain not one but several avalanche mechanisms.<sup>31</sup> This is particularly pertinent for metals and alloys. A typical example is the case of Ho-bearing alloys where the compression and tension mechanisms contain superposition of dislocation movements and

porous collapse.<sup>25</sup> Each mechanism generates its own avalanche system with some, often weak, interactions between them.

Experimental observations of the coincidence of complex subsystems are usually hampered in ductile alloys, such as stainless steel, because their AE strength is weak, and the avalanches are sparse and do not lend themselves to a full avalanche analysis. In particular, alloys with a fcc structure are usually very ductile and few studies succeeded in characterizing crackling noise in these compounds. The surprising observation<sup>23</sup> was that those few AE signals, which can be measured in fcc metals, follow the same avalanche statistics as those of brittle materials. There are simply fewer avalanches, but they are not thought to be different from those in alloys with a hcp structure. We show in this paper that several avalanche mechanisms coincide for a fcc alloy. We demonstrate that we can disentangle the mechanisms in several ways, namely, by separating multivalued  $E \sim A^2$  scalings and by different avalanche durations at the same amplitudes.

We used austenitic stainless steel for this study because it is widely used in food processing, petrochemical and nuclear industries, and aerospace applications with high resistance to corrosion and oxidation.<sup>32,33</sup> Traditional austenitic stainless steel shows relatively low yield strengths.<sup>34</sup> Our 316L stainless steel contains 2%–3% of Mo, which reduces the mobility of dislocations. This reduced mobility makes 316L SS much easier to work-harden during deformation processing. Their microstructural, magnetic, mechanical, and corrosion properties are well documented.<sup>24,35–45</sup>

The ingot cold rolled stainless steel 316L sheet was cut with a wire-saw into dog-bone shaped samples with a gauge range of 25 mm × 4 mm × 1.5 mm. Uniaxial tensile experiments on steel samples were performed on an Instron5969 Universal Testing system with a tensile rate of 0.01 mm/min at room temperature. Acoustic emission signals were recorded during a tensile process by using a piezoelectric sensor (Vallen-Systeme GmbH) with a frequency range of 200–800 kHz. The recording signals were first pre-amplified by 49 dB and then transferred for a waveform analysis using a AMSY-6 AE-measurement system (Vallen-Systeme GmbH) with a frequency range of 95–850 kHz. The amplitude  $A$  is recorded in dB, which follows the expression  $\text{dB} = [20 \text{ Log } (|V_{\text{sensor}}|/1 \mu\text{V})]$ , where  $V_{\text{sensor}}$  is the peak voltage output by the sensor, and the brackets indicate the value to its nearest integer in dB. An AE signal is defined as a “burst” in the noise spectrum. The start of a burst is determined by a first threshold crossing and ended at second threshold crossing or when duration discrimination time (DDT defines a time period in which no threshold crossing must occur in order that an end of hit is determined) expired without any threshold crossing. A threshold of 21.1 dB was determined by a tension experiment where the metal sample was replaced by rubber. The detectors were attached to the rubber sample.<sup>25</sup> This experiment allowed us to measure the noise of the experimental arrangement without the AE effect of the metal sample. For details, see Ref. 25. Prior to the full tension experiment, we performed tensile experiments with similar samples but different DDTs (which ranges from 50  $\mu\text{s}$  to 1000  $\mu\text{s}$ ) and found that  $\text{DDT} \sim 100 \mu\text{s}$  fits the dislocation movements in the present material very well. The way how we record the acoustic emission events and define the amplitude, duration, and energy is shown in the [supplementary material](#) (Fig. S1).

Figure 1 shows the strain–stress curve together with the AE signals obtained during tension. The cold rolled sample was stretched with a rate of  $1 \times 10^{-2}$  mm/min, and the failure point is 650 MPa with

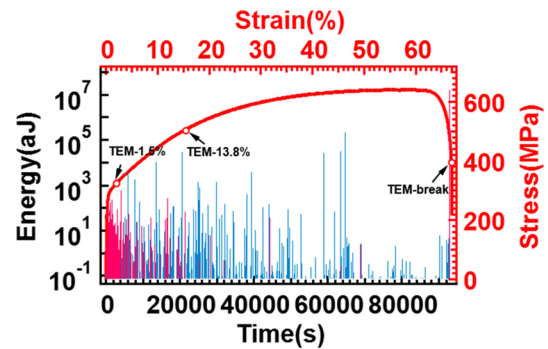
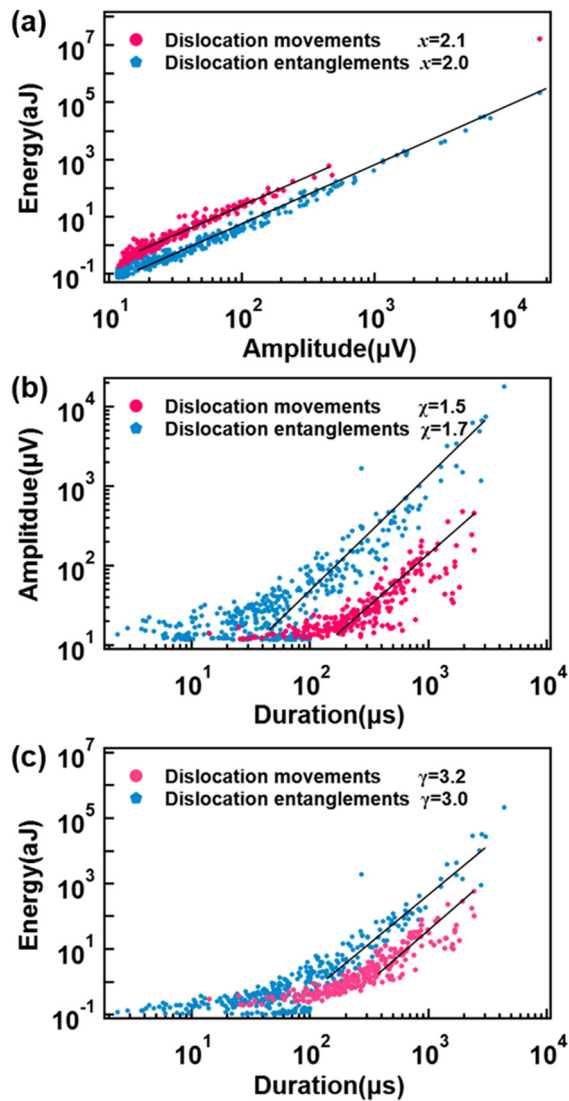


FIG. 1. Strain–stress curve with AE signals for the cold rolled sample under tension with a rate of  $1 \times 10^{-2}$  mm/min. The two jerk populations are colored in red (dislocation movements) and blue (dislocation entanglements). Dislocation movements dominate for weak tension, and dislocation entanglements dominate near the final break point. The two populations are separated in Figs. 2 and S2.

a maximum strain of 68%. The AE signals are non-stationary with a concentration of jerks in the beginning of the experiment and near the critical breaking point. We first analyze the correlation between the energy and the maximum amplitude of each avalanche. The energy is defined as the integral over the squared amplitude  $A(t)$ , integrated over the duration of the avalanche:  $E \sim \int_0^D A(t)^2 dt$ . If the durations of two superposed processes differ greatly, then this discrepancy can be seen in the correlation  $E(A)$  because AE signals with longer durations show larger energies for the same maximum amplitude  $A$  than those for shorter durations.

The three key correlations of AE spectra are shown in Fig. 2, namely, energy vs amplitude  $E(A)$ , amplitude vs duration  $A(D)$ , and energy vs duration  $D(E)$ . The correlation  $E(A)$  contains two linear branches in log–log representation with the same scaling exponent  $x=2$  in  $E \sim A^x$  [Fig. 2(a)]. The value  $x=2$  is typical for AE experiments.<sup>27</sup> A similar shift between two populations appears in  $A(D)$  [Fig. 2(b)]. For longer durations, we find power law scaling  $A \sim D^\chi$ , where  $\chi$  varies between 1.5 and 1.7, which is near the MF value of 1.5.<sup>26,27</sup> The  $E(D)$  correlation also shows two branches in Fig. 2(c) with their related exponent  $\gamma$  in  $E \sim D^\gamma$  between 3 and 3.2, which is remarkably close to the MF value of 3.<sup>46</sup> Most importantly, Fig. 2 indicates that the difference between the two branches is related to different avalanche durations. This observation allows us to distinguish between the two processes.

Avalanches with long durations dominate the early stages of the tension experiments (Fig. 1). Transmission electron microscopy (TEM) observations show dislocations at early stages of tension, while dislocation entanglements dominate the later stages ([supplementary material](#), Fig. S2). We conclude that datasets with long durations relate to dislocation movements and those with short durations are due to dislocation entanglements. The same differentiation is possible by analyzing the probability distribution function of AE durations: individual dislocations show longer AE durations than dislocation entanglements ([supplementary material](#), Fig. S4). We note that the two branches in  $E(A)$ ,  $A(D)$ , and  $E(D)$  curves are very distinct when the amplitude is larger than 20  $\mu\text{V}$  (Fig. 2), and this phenomenon is reproducible no matter how we change the sample size and the frequency of the detector. We compare samples with different widths and lengths. For each



**FIG. 2.** (a) Energy vs amplitude correlations for dislocation movements and entanglements show an exponent  $x = 2.0 \pm 0.1$ , (b) amplitude vs duration correlations for dislocation movements and entanglements show an exponent  $\chi = 1.5 \pm 0.2$ , and (c) energy vs duration correlation dislocation movements and entanglements. The exponent is  $\gamma = 3.0 \pm 0.2$ .

size, we measured the AE signals by three different detectors (supplementary material, Fig. S5). We repeated the experiment five times (supplementary material, Table S1) and found no significant variations (supplementary material, Fig. S3).

We now analyze the two populations separately and determine their avalanche energies. We plot the probability distribution function (PDF) of the energy of two subgroups with long durations (dislocation movements) and short durations (entanglements) together with overall signals for all AE signals in Fig. 3.

The probability distribution functions, PDFs, are defined as the number of events in a given energy range per bin width divided by the

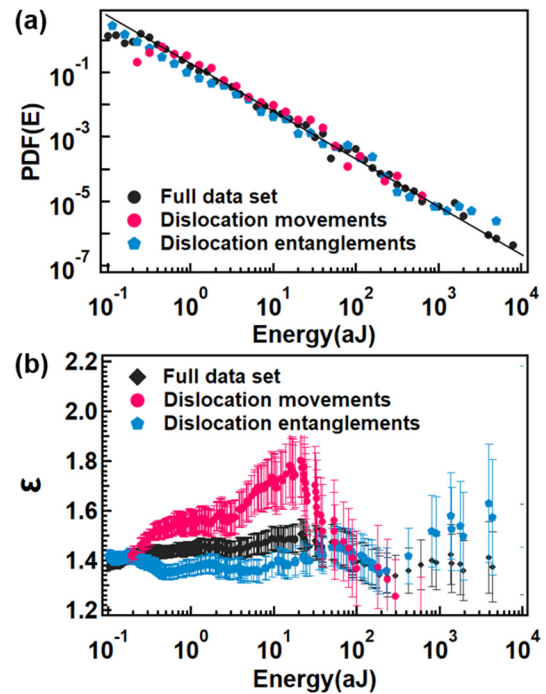


**FIG. 3.** (a) Probability distribution of the dislocation movements (red), dislocation entanglements (blue), and the full dataset (black). (b) The maximum likelihood (ML) estimates show differences between the three datasets with  $\varepsilon = 1.55$  (dislocation movements), 1.36 (entanglements), and 1.45 for the combined dataset.

total number of events. The power laws in Fig. 3 have slightly smaller exponents for entanglements than for dislocation movements. The total dataset lies roughly in the middle of the two extreme cases. The complement cumulative distribution functions<sup>7</sup> are shown in the supplementary material, Fig. S6.

The jerk spectra were then analyzed using the maximum likelihood (ML) method.<sup>47</sup> The ML curves in Fig. 3(b) confirm that the energy exponents are slightly different for the two populations and the combined spectra:  $\varepsilon = 1.55$  (dislocation movements), 1.36 (entanglements), and 1.45 for the combined dataset.

We measured a large number of AE signals to identify the two deformation mechanisms of 316L stainless steel due to their different avalanche durations. The AE signals of dislocation movements are concentrated near the initial state, near the yield point, and near the final collapse. We then characterize the local evolution of the microstructure by transmission electron microscopy (TEM) of the same samples as used for the AE experiments (see the list of samples in the supplementary material and Fig. S2). The TEM pattern of the virgin samples [Fig. S2(a)] shows few dislocations. A strong increase in the dislocation density [Fig. S2(b)] occurs in the yield regime with a macroscopic strain of 1.5%. This indicates a regime of dislocation nucleation and growth. Further tension leads to both dislocation nucleation/growth and dislocation entanglements [Fig. S2(c)]. Dense dislocation entanglements [Fig. S2(d)] appear near and after the failure point. The strain values of the TEM observations are indicated in Fig. 1. By comparing the AE signals with the electron-microscopic images, we confirm the origin of two avalanche processes from

dislocation movements (including nucleation and growth) and from dislocation entanglements (tangle-detangles). We have not followed *in situ*-scanning electron microscope, which could potentially provide direct evidence of the active deformation mechanisms<sup>48</sup> because it is insensitive to the observation of the evolution of local dislocations.

The differences between durations of the two populations are also found in the AE waveforms of individual avalanches. The waveforms with various maximum amplitudes are shown in the [supplementary material](#), Fig. S7, and the waveform with different durations and the comparison with graphite rod test are shown in the [supplementary material](#), Figs. S8–S11. Two typical waveforms with similar maximum amplitudes around  $200\ \mu\text{V}$  are shown in Fig. 4. From these profiles, we conclude that signals of an initial dislocation nucleation and growth decay roughly three times more slowly than entanglement avalanches. The average duration for all signals is  $553\ \mu\text{s}$  for dislocation movements and  $188\ \mu\text{s}$  for entanglements. Only one event determines the waveform of dislocation entanglements. This is in contrast to the waveform of dislocation movements, which always contain multiple overlapping events. We conclude that the changes of the event durations reflect the movement of preexisting dislocations as shown in Fig. S2. The initial dislocation triggers the movements of other preexisting dislocations. Their avalanche profiles overlap, forming extremely long AE signals.

AE profiles are compared for all signals in Fig. S12 ([supplementary material](#)) where the maximum amplitudes are normalized to unity and the decays of the envelop of the AE signals are plotted as a function of time. In the elastic regime, at the early stages of the tension experiment, we find that signals terminate before 2 ms and that the

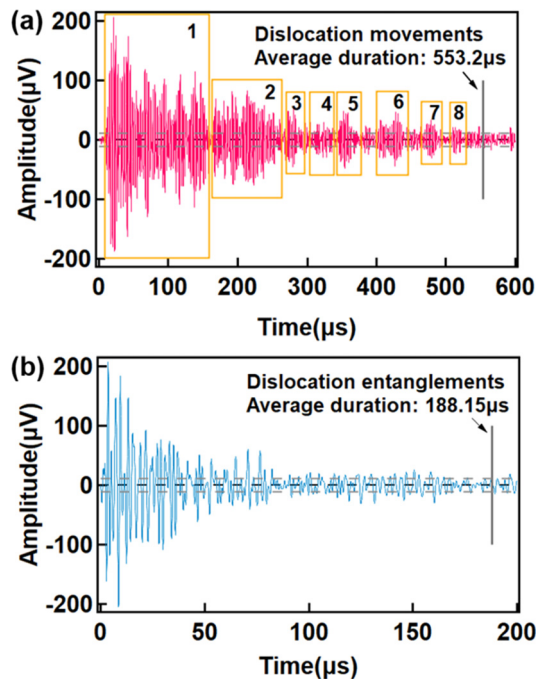


**FIG. 4.** Acoustic waveform and frequency spectrum of dislocation movements (a) and dislocation entanglements (b) with maximum amplitudes near  $200\ \mu\text{V}$ . In (a), a rough assignment of the triggered avalanches 1–8 is shown in yellow boxes.

profiles are statistically identical for the dislocation movements ([supplementary material](#), Fig. S12). In the plastic regime, the dislocation slips generate signals with durations of some 2 ms and a slow decay; the decay time to 1/100 of the maximum amplitude is ca. 2 ms. Dislocation entanglements persist until 4.5 ms with a much shorter decay time to 1/100 of 0.2 ms ([supplementary material](#), Fig. S12).

These times are now compared with the waiting times for avalanche. Waiting times are power law distributed (Fig. 5) for short waiting times  $< 1\ \text{s}$ . Aftershocks are seen for the shortest time spans  $< 0.5\ \text{ms}$ , which are comparable with the average duration of dislocation avalanches. This observation suggests that many of the local maxima during the profile decay in Fig. 4(a) are in fact small aftershocks, which could not be separated by the AE experiments. This observation implies that dislocation aftershocks are triggered by the mainshock,<sup>49</sup> contributing to the same AE signal.

The slope of the power law for the waiting times is  $-0.89$ , which is close to the mean field value of  $-1$ . The probability distribution is very similar for aftershocks (Omori law) for the initial event of a moving dislocation and a changing entanglement. The cross correlation between dislocation movements and entanglements is in the same order of magnitude as the aftershocks of the same species. In Fig. S13 ([supplementary material](#)), we show that the average rate of dislocation entanglements after a main shock of dislocations follows the same trend as the rate of dislocation movements after an entanglement main shock. Similar trigger events have been reported in metal single crystals<sup>49,50</sup> and an analysis is described in Ref. 51, where similar time clustering of AE events, i.e., high aftershock activity, was reported.

Our results show that AE spectra in stainless steel hide in their fine structure two species of avalanches. Similar superposition effects are common in many materials,<sup>30</sup> but their discovery is beset by experimental difficulties. In some systems, the various species show very different energy exponents and, hence, other related exponents for amplitudes, which makes it easy to separate the contributing mechanisms.<sup>25</sup> In other cases, a separation is possible because the PDF and ML curves of the two mechanisms show fingerprints like bending and oscillations,<sup>52</sup> which allows us to estimate the energy exponents of each mechanism in some approximation. A subtler and more complex indicator for superpositions is related to the durations and the profiles

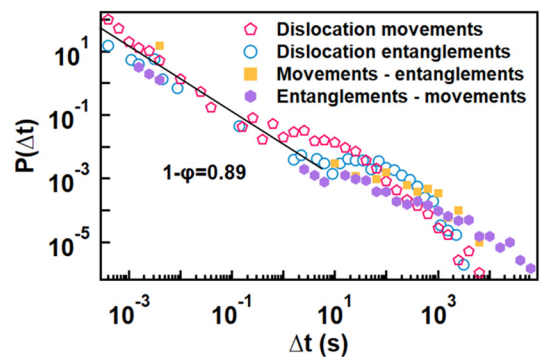


**FIG. 5.** Waiting time distributions for four datasets. Dislocation movements and entanglements show strong correlations up to time delays of 1 s. For longer time delays, the distribution is randomized. Trigger events where dislocation movements trigger entanglements are rare, while entanglements commonly trigger dislocation movements.

of AE signals. Here, we have shown that an excellent fingerprint for the detection of coincidences between two mechanisms is the observation of a multivalued  $E \sim A^2$  correlation. If the lifetimes of individual AE signals are different for the two processes involved, the longer lifetimes shift the  $E(A)$  correlation to higher energies. This effect is seen in Fig. 2(a) where the two branches of the scaling relationship demonstrate the multivalued scaling. This very simple fingerprint shows that avalanches are related to two different mechanisms in stainless steel. In several independent experiments, we have shown before that in the overwhelming majority of cases, this is not the case. In these “normal” scenarios, we see only a single valued  $E \sim A^2$  relationship.<sup>22,25</sup> The fact that two branches in the  $E \sim A^2$  relation appear in the current case was unexpected and reveals the potentially complex nature of superposed avalanche mechanisms.

Our method is useful not only for metals and alloys but also equally for ceramics and for the analysis of switching processes in ferroic materials. As described in detail in Ref. 53, other possible consequences of systematic differences between the lifetimes of different avalanche species are expected to include a stronger asymmetry of avalanche profiles of one species compared with the other. Further work is planned on this topic.

See the [supplementary material](#) for the complete analysis of acoustic waveforms and experimental details.

Financial support from the National Natural Science Foundation of China (Nos. 51931004 and 51621063) and 111 project 2.0 (No. BP2018008) is gratefully acknowledged. E. K. H. Salje is grateful to EPSRC (No. EP/P024904/1). Y. Chen was supported by a scholarship from the China Scholarship Council to visit the University of Cambridge.

## DATA AVAILABILITY

The data that support the findings of this study are available from the corresponding author upon reasonable request.

## REFERENCES

- K. A. Dahmen, Y. Ben-Zion, and J. T. Uhl, *Phys. Rev. Lett.* **102**, 175501 (2009).
- P. D. Ispanovity, L. Laurson, M. Zaiser, I. Groma, S. Zapperi, and M. J. Alava, *Phys. Rev. Lett.* **112**, 235501 (2014).
- E. Vives, J. Baro, M. C. Gallardo, J. M. Martin-Olalla, F. J. Romero, S. L. Driver, M. A. Carpenter, E. K. H. Salje, M. Stipcich, R. Romero, and A. Planes, *Phys. Rev. B* **94**, 024102 (2016).
- J. Baro, A. Planes, E. K. H. Salje, and E. Vives, *Philos. Mag.* **96**, 3686 (2016).
- F. J. Romero, J. M. Martin-Olalla, M. C. Gallardo, D. Soto-Parra, E. K. H. Salje, E. Vives, and A. Planes, *Phys. Rev. B* **99**, 224101 (2019).
- E. K. H. Salje, J. Koppensteiner, M. Reinecker, W. Schranz, and A. Planes, *Appl. Phys. Lett.* **95**, 231908 (2009).
- N. Friedman, A. T. Jennings, G. Tsekenis, J. Y. Kim, M. L. Tao, J. T. Uhl, J. R. Greer, and K. A. Dahmen, *Phys. Rev. Lett.* **109**, 095507 (2012).
- D. Soto-Parra, X. X. Zhang, S. S. Cao, E. Vives, E. K. H. Salje, and A. Planes, *Phys. Rev. E* **91**, 060401 (2015).
- J. Baro, J. M. Martin-Olalla, F. J. Romero, M. C. Gallardo, E. K. H. Salje, E. Vives, and A. Planes, *J. Phys.: Condes. Matter* **26**, 125401 (2014).
- M. C. Gallardo, J. Manchado, F. J. Romero, J. del Cerro, E. K. H. Salje, A. Planes, E. Vives, R. Romero, and M. Stipcich, *Phys. Rev. B* **81**, 174102 (2010).
- E. K. H. Salje, H. Zhang, H. Idrissi, D. Schryvers, M. A. Carpenter, X. Moya, and A. Planes, *Phys. Rev. B* **80**, 134114 (2009).
- E. K. H. Salje, H. Zhang, A. Planes, and X. Moya, *J. Phys.: Condes. Matter* **20**, 275216 (2008).
- J. Weiss, T. Richeton, F. Louchet, F. Chmelik, P. Dobron, D. Entemeyer, M. Lebyodkin, T. Lebedkina, C. Fressengeas, and R. J. McDonald, *Phys. Rev. B* **76**, 224110 (2007).
- J. Baro, A. Corral, X. Illa, A. Planes, E. K. H. Salje, W. Schranz, D. E. Soto-Parra, and E. Vives, *Phys. Rev. Lett.* **110**, 088702 (2013).
- J. Baro, P. Shyu, S. Y. Pang, I. M. Jasiuk, E. Vives, E. K. H. Salje, and A. Planes, *Phys. Rev. E* **93**, 053001 (2016).
- G. F. Nataf, P. O. Castillo-Villa, J. Baro, X. Illa, E. Vives, A. Planes, and E. K. H. Salje, *Phys. Rev. E* **90**, 022405 (2014).
- G. F. Nataf, P. O. Castillo-Villa, P. Sellappan, W. M. Kriven, E. Vives, A. Planes, and E. K. H. Salje, *J. Phys.: Condes. Matter* **26**, 275401 (2014).
- P. O. Castillo-Villa, J. Baro, A. Planes, E. K. H. Salje, P. Sellappan, W. M. Kriven, and E. Vives, *J. Phys.: Condes. Matter* **25**, 292202 (2013).
- E. K. H. Salje, D. E. Soto-Parra, A. Planes, E. Vives, M. Reinecker, and W. Schranz, *Philos. Mag. Lett.* **91**, 544 (2011).
- E. K. H. Salje, G. I. Lampronti, D. E. Soto-Parra, J. Baro, A. Planes, and E. Vives, *Am. Mineral.* **98**, 609 (2013).
- T. Beirau and E. K. H. Salje, *Appl. Phys. Lett.* **115**, 071902 (2019).
- Y. Chen, Q. B. Wang, X. D. Ding, J. Sun, and E. K. H. Salje, *Appl. Phys. Lett.* **116**, 111901 (2020).
- J. Weiss, W. Ben Rhouma, T. Richeton, S. Dechanel, F. Louchet, and L. Truskinovsky, *Phys. Rev. Lett.* **114**, 105504 (2015).
- S. G. Chowdhury, S. Das, and P. K. De, *Acta Mater.* **53**, 3951 (2005).
- Y. Chen, X. D. Ding, D. Q. Fang, J. Sun, and E. K. H. Salje, *Sci. Rep.* **9**, 1330 (2019).
- E. K. H. Salje and K. A. Dahmen, in *Annual Review of Condensed Matter Physics*, edited by J. S. Langer (Annual Reviews, Palo Alto, 2014), Vol. 5, p. 233.
- E. K. H. Salje, D. Xue, X. Ding, K. A. Dahmen, and J. F. Scott, *Phys. Rev. Mater.* **3**, 014415 (2019).
- X. Jiang, D. Y. Jiang, J. Chen, and E. K. H. Salje, *Am. Miner.* **101**, 2751 (2016).
- X. Jiang, H. L. Liu, I. G. Main, and E. K. H. Salje, *Phys. Rev. E* **96**, 023004 (2017).
- E. K. H. Salje, H. L. Liu, L. S. Jin, D. Y. Jiang, Y. Xiao, and X. Jiang, *Appl. Phys. Lett.* **112**, 054101 (2018).
- E. K. H. Salje, H. L. Liu, Y. Xiao, L. S. Jin, A. Planes, E. Vives, K. N. Xie, and X. Jiang, *Phys. Rev. E* **99**, 023002 (2019).
- C. Donadille, R. Valle, P. Dervin, and R. Penelle, *Acta Metall.* **37**, 1547 (1989).
- P. M. D. Silva, H. F. G. de Abreu, V. H. C. de Albuquerque, P. D. Neto, and J. Tavares, *Mater. Des.* **32**, 605 (2011).
- M. F. Ashby and D. Cebon, *J. Phys. IV* **3**, 1 (1993).
- V. Seetharaman and R. Krishnan, *J. Mater. Sci.* **16**, 523 (1981).
- S. Kheiri, H. Mirzadeh, and M. Naghizadeh, *Mater. Sci. Eng. A* **759**, 90 (2019).
- S. Tanhaei, K. Gheisari, and S. R. A. Zaree, *Int. J. Miner. Metall. Mater.* **25**, 630 (2018).
- S. Li, B. Gao, Z. W. Huang, H. Zhou, Q. Z. Mao, and Y. S. Li, *Vacuum* **157**, 128 (2018).
- Q. Y. Long, J. X. Lu, and T. H. Fang, *Mater. Sci. Eng. A* **751**, 42 (2019).
- D. N. Wasnik, I. K. Gopalakrishnan, J. V. Yakhmi, V. Kain, and I. Samajdar, *ISIJ Int.* **43**, 1581 (2003).
- B. R. Kumar, *J. Mater. Sci.* **45**, 2598 (2010).
- L. Xiong, Z. S. You, S. D. Qu, and L. Lu, *Acta Mater.* **150**, 130 (2018).
- B. Wilshire and M. Willis, *Metall. Mater. Trans. A* **35**, 563 (2004).
- N. Nakada, H. Ito, Y. Matsuoka, T. Tsuchiyama, and S. Takaki, *Acta Mater.* **58**, 895 (2010).
- D. Raabe, *Acta Mater.* **45**, 1137 (1997).
- J. Baro and J. Davidsen, *Phys. Rev. E* **97**, 033002 (2018).
- A. Clauset, C. R. Shalizi, and M. E. J. Newman, *SIAM Rev.* **51**, 661 (2009).
- D. Drozdenko, J. Capek, B. Clausen, A. Vinogradov, and K. Mathis, *J. Alloy. Compd.* **786**, 779 (2019).
- T. Richeton, P. Dobron, F. Chmelik, J. Weiss, and F. Louchet, *Mater. Sci. Eng. A* **424**, 190 (2006).
- J. Weiss and D. Marsan, *Science* **299**, 89 (2003).
- J. Weiss and M. C. Miguel, *Mater. Sci. Eng. A* **387**, 292 (2004).
- E. K. H. Salje, A. Planes, and E. Vives, *Phys. Rev. E* **96**, 042122 (2017).
- C.-C. Vu and J. Weiss, *Phys. Rev. Lett.* **125**, 105502 (2020).